Deformability of Filament-Wound GFRP Tubes Filled with Lightweight Aggregate Concrete: Experimental and Improved Analytical Studies

Kraig Bates and Pedram Sadeghian

Department of Civil and Resource Engineering, Dalhousie University, Halifax, NS, Canada

Abstract:

Previous research indicates that lightweight aggregate (LWA) concrete exhibits more brittle failure under compression than conventional normal density (ND) concrete. In contrast, angle-ply fiber-reinforced polymer (FRP) filament-wound tubes filled with ND concrete show significant improvements in strength and deformability compared to hollow tubes. This study evaluates the impact of these tubes on LWA concrete to mitigate its brittle behavior. Sixteen concrete-filled FRP filament-wound tubes (CFFTs) made of ±55° filament-wound glass FRP (GFRP) were tested under axial compression. The GFRP tube's mechanical properties and fiber winding angle of ±55º allowed for a compressive strength enhancement factor ranging from 2 to 5 for the CFFTs compared to unconfined specimens. Results also revealed substantial nonlinearity and deformability in the LWA-CFFTs due to the angle-ply tube orientation. An iterative analytical model predicted the CFFT's nonlinear response, validated by experimental data. The findings demonstrate that angle-ply FRP tubes effectively enhance the bearing capacity and deformability of inherently brittle unconfined LWA concrete.

KEYWORDS: Filament-wound; GFRP; tube; lightweight; concrete; CFFT.

DOI: https://doi.org/10.1177/00219983241295809

1 INTRODUCTION

The use of prefabricated filament-wound fiber-reinforced polymer (FRP) tubes in concrete-filled FRP tubes (CFFTs) as external reinforcement for concrete cores has gained considerable attention [1][2][3]. CFFTs distinguish themselves from FRP-wrapped concrete columns by exhibiting significant axial stiffness inherent in the FRP tube itself. When assessing the axial capacity of a CFFT column, a more accurate approach involves considering the biaxial state of stress in both axial and hoop directions of the FRP tube [4][5][6]. Various factors, including the mechanical properties and the filament winding angle of the FRP tube in relation to the loading direction, can influence the bearing capacity of a CFFT [7][8][9].

Regarding the biaxial state of stress imposed on the FRP tubes in a CFFT, Fam and Rizkalla [4] proposed an iterative model for analyzing the axial load vs. both axial and hoop strain responses of a CFFT by considering force equilibrium and radial displacement compatibility at the concrete core-FRP tube interface due to biaxial tube action. The model predicts the behavior of CFFTs made of a near-cross-ply FRP tube very well. A near-cross-ply FRP tube is defined where the fibers are predominantly oriented in the longitudinal and circumferential directions of the tube (e.g., +85°/-5° with respect to the axial direction of the tube) [10].

However, some FRP tubes in the market with larger fiber angle orientation, for example ±55° angle-ply tubes [11][12], which behave differently than the cross-ply tubes [10], particularly if the tube is filled with concrete[13]. Jawdhari et al. [13] demonstrated that an angle-ply tube-filled with concrete exhibits a notable increase in both tensile strength and stiffness compared to its hollow counterpart. The presence of concrete core places the tube in a state of biaxial tensile stress, resulting in a failure envelope from this stress combination significantly exceeds the uniaxial

strength in either axial or hoop direction. The nonlinear behavior of angle-ply CFFTs is evident, and it is captured using a finite element analysis [13].

Recently, Xie et al. [6] developed a theoretical model for CFFTs subjected to axial compression, incorporating the nonlinear biaxial characteristics of the FRP confining tube. Two existing models by Hahn and Tsai [14] and Jones and Nelson [15] were used to describe the nonlinear behavior of FRP confining tubes, both of which were incorporated into the stress-strain model developed by Jiang and Teng [16] for FRP-confined concrete, using a nonlinear biaxial model for the FRP confining tube. The studies mentioned above demonstrate that CFFTs composed of angle-ply tubes exhibit substantial nonlinear behavior, indicating significant deformability for the system.

While the deformability of angle-ply tubes filled with normal weight concrete has been studied, the influence of lightweight concrete on the nonlinear behavior of concrete-filled angle-ply tubes remains unexplored. Lightweight concrete, particularly lightweight aggregate (LWA) concrete, offers distinct advantages such as reduced structural dead load and improved thermal insulation properties, making it a promising material for construction applications. Given the brittle behavior of unconfined LWA concrete, understanding the effects of angle-ply tubes on the deformability of confined LWA concrete is crucial for optimizing their structural design and performance in practical engineering scenarios.

Extensive research suggests that LWA concrete specimens tend to fail in a more brittle manner than conventional normal density (ND) concrete under compression [17][18][19]. One significant source of the increased brittleness observed in LWA concrete is attributed to the lower stiffness associated with coarse LWA compared to the surrounding cement matrix. When subjected to compressive loading, the coarse LWA often becomes the initial site of cracking, which initiates fracturing within the cement matrix [17]. Under uniaxial compression, the fracture path in LWA

concrete specimens advances through the aggregate, whereas for ND concrete specimens, the fracture path trends around the aggregates at the aggregate-matrix interface, which creates a rougher failure plane, as shown in Figure 1a. In contrast, the smooth fracture path in LWA concrete specimens produces a rapid decline in the axial stress-strain curve after reaching their post-peak compressive strength, as illustrated in Figure 1b. The protruding aggregates along the fracture path observed in ND concrete specimens from compression failure can interlock with the opposing portion of concrete, significantly increasing its ductility. This phenomenon is often characterized by a gradual decline in the stress-strain curve after the peak, prior to ultimate failure [17][20].

Given that angle-ply FRP tubes have significantly enhanced the strength and deformability of ND concrete [6][13], the current research evaluates the influence of these tubes on LWA concrete to mitigate the brittle post-peak strength behavior observed in unconfined LWA concrete. This study compares the experimental compressive load-strain behavior of CFFTs made of ND and LWA concrete, and a theoretical model is implemented to predict the axial compressive behavior of the CFFTs based on the mechanical properties of both the concrete core and the FRP tube.

2 EXPERIMENTAL PROGRAM

2.1 Test Matrix and Materials

The experimental program began with the development of a testing plan and the fabricating a sufficient and comparable number of test specimens. The primary test specimens used in this research were unconfined concrete cylinders and CFFT specimens. Unconfined concrete cylinders were fabricated using both lightweight aggregate (LWA) concrete and normal density (ND) concrete, with two different form dimensions: 76.2×152.4 mm and 101.6×203.2 mm, corresponding to a 2:1 length-to-diameter (aspect) ratio.

Two types CFFTs were fabricated, utilizing both LWA concrete and ND concrete as the core. The first group consisted of thin-walled GFRP tube sections with an inner diameter of 76.2 mm and an average wall thickness of 1.87 mm, resulting in a D/t ratio of 40.7. The second group comprised thick-walled GFRP tube sections with an inner diameter of 76.2 mm and an average wall thickness of 4.03 mm, resulting in a D/t ratio of 18.9. All GFRP tube sections sourced from prefabricated GFRP pipes, which were supplied by a local manufacturer (RPS Composites, Mahone Bay, NS, Canada). The diameter of the tubes was determined by the availability of the manufacturer's products at the time of the research and the capacity limitations of the testing machine.

The nominal internal pressure rating of the thin-walled and thick-walled GFRP pipes were reported by the manufacturer as 50 psi (~350 kPa) and 150 psi (~1050 kPa), respectively. The GFRP tubes are composed of Bisphenol-A based epoxy vinyl ester resin and E-CR glass fiber roving. The GFRP tubes consist of a $\pm 55^{o}$ filament winding structure in reference to the longitudinal direction of the pipe [11]. The material properties are presented in Table 1, which was obtained based on material composition and for a volume-fiber fraction of 55% [11].

A $\pm 55^{o}$ fiber orientation is the most common design in the pipe industry, as it provides balanced strength in both axial and circumferential directions, in line with pressure vessel theory. This orientation allows designers to use standard, off-the-shelf products rather than resorting to custom-manufactured fiber orientations, which could raise the overall cost of the CFFT system. Potential trade-offs compared to other orientations include the fact that the $\pm 55^{o}$ orientation makes the tubes twice as strong in the circumferential direction as in the axial direction, offering strong confinement for the concrete core while also providing axial strength and stiffness for the CFFT.

For both LWA concrete and ND concrete mixes, three 76.2×152.4 mm and six 101.6×203.2 mm unconfined concrete cylinders were cast using prefabricated plastic molding. Regarding the CFFTs, four different groups of CFFTs were constructed and analyzed, which consisted of four specimens for each category. The CFFT categories included both thin-walled and thick-walled GFRP tubes filled with either LWA concrete or ND concrete. To distinguish specimens' groups, a specific name convention was used for the unconfined concrete cylinders and the CFFT specimens. The unconfined concrete cylinder used: UCA-28(B), where A is the type of concrete (i.e., LWA or ND), and B is the size of the specimen (i.e., S refers to the smaller specimens and L refers to the larger specimens). Parameter UC in the following name convention refers to unconfined, and 28 refers to the curing period in terms of days. As an example, a group of the smaller dimension unconfined LWA concrete cylinders would be identified as UCLWA-28(S).

The CFFTs followed a similar notation: XCFFT-PY, where X refers to the type of concrete (i.e., LWA or ND), and B refers to the internal pressure rating of the external GFRP tube (i.e., thin-walled tubes are rated at 50 psi, and thick-walled tubes are rated at 150 psi). As an example, a thin-walled CFFT consisting of a cast-in-place ND concrete core would be identified as NDCFFT-P50. The test matrix, which includes specimen grouping, specimen quantity, FRP layers within laminate stacking sequence, relative specimen dimensions (i.e., height to outer diameter aspect ratio of 2:1), and the GFRP tube layup code from the filament winding process is presented in the test matrix in Table 2.

2.2 Concrete Mix Design and Production

The normal density concrete mix design was derived in accordance with ACI 211.1-22 [21] for a desirable compressive strength of concrete (i.e., 25-30 MPa). It was batched using four constituents, fine aggregate (sand), coarse aggregate with a nominal maximum size of 12.7mm,

QUIKCRETE Portland cement Type 10-F, and water. The lightweight aggregate concrete mix design was derived using ACI 211.2-98 [22] to produce a mix of similar strength to the normal density concrete for comparative purposes. The lightweight coarse aggregate used in this experiment was 9.5mm (3/8-inch) Norlite expanded shale aggregate, which was provided by Norlite LLC (Cahoes, NY, United States of America). The elastic modulus of concrete, E_c, of was obtained for both types of concrete through ACI 318-14 [23] using Eq. 1

$$E_c = 0.043\omega^{1.5}\sqrt{f_c'} \quad (1)$$

where, ω is the unit weight (kg/m^3) of the concrete core, and f_c' is the compressive strength (MPa) of concrete core. Per ACI 318-14 [23], this expression is valid for estimating the modulus of elasticity of concrete, E_c, for concrete with densities between 1440 and 2480 kg/m^3 and for compressive strength ranging up to 35 MPa. Therefore, Eq. 1 may be utilized to estimate E_c for both ND and LWA concrete for this research, and values are presented in Table 1. The unconfined compressive strength of both LWA and ND concrete was taken as the average value determined from the experimental displacement-controlled axial compression results on the unconfined cylinders, which is also presented in Table 1. The lightweight porous ceramic aggregate is produced by placing select shale through a vitrification and expansion process. Select shale is placed in a rotary kiln which is heated up to temperatures exceeding 1200°C, where the aggregates begin to liquify (vitrify) and expanded due to the release of carbonadoes gas within the original aggregate material [24]. The expanded product is then cooled by air, forming the porous material. The lightweight aggregate concrete mix used the same type of cement fine aggregate as the normal density concrete mix. The fine aggregate used to produce both lightweight aggregate concrete and normal density concrete was provided by Casey Metro Ltd. (Bedford, NS, Canada), specifically for the purpose of this research. The batching procedure for both types of concrete was completed

in two phases. The first phase was implemented to ensure that both the LWA and ND concrete mix designs fell within the desired range and had similar compressive strengths. This comparability was essential for achieving similar unconfined stress-strain behavior in both types of concrete. Variations in mix design that lead to significant differences in compressive strength between LWA and ND concrete are critical factors influencing the axial load capacity of CFFT systems. The second phase was executed to produce the experimental unconfined concrete cylinders and the CFFTs.

2.3 CFFT Production

The GFRP tubes were cut into sections with an aspect ratio slightly larger than 2:1 (i.e., 180mm in length). Caulking was used to attach the bare GFRP tubes to a nonabsorbent (plastic-wrapped) piece of plywood to create a tight seal and flat surface at the interface to mitigate leakage or absorption of bleed water required for concrete hydration. Upon completion of the phase 2 batching process for both types of concrete, the fresh concrete was directly cast within the GFRP tube apparatus and plastic concrete cylinder molding to produce the CFFTs and unconfined concrete cylinders, respectively. For each specimen, the concrete was placed in three even layers and rodded 25 times for proper distribution and compaction per ASTM C31. After the initial concrete curing period, both the unconfined cylinders and CFFT specimens were placed in a temperature-controlled moisture room for 28 days to complete the required concrete hydration cycle per ASTM C31. Once the concrete specimens completed the curing cycle, the CFFTs were end-grinded to a 2:1 aspect ratio (i.e., 152.4×76.2 mm) for the compression testing purposes[25].

For both LWA and ND unconfined concrete specimens, three 76.2×152.4 mm and three 102.4×203.2 mm cylinders were cast in phase 1 of the mixing trial for strength comparison purposes. It was determined in this phase that both specimens had approximately the same

compressive strength from load-controlled testing at 0.35 MPa/sec. This was completed for both lightweight aggregate and normal density concrete mixes. In phase 2 of the mixing process, only three 102.4x203.2mm unconfined cylinders were constructed for each mix type. These concrete cylinders were used to analyze the displacement-controlled stress-strain response due to constraints with the smaller unconfined concrete specimens (i.e., 76.2×152.4 mm) rigidly attaching to the CFFT-linear potentiometer yoke apparatus. The load vs. biaxial displacement data obtained from experimental testing was then scaled to represent the smaller 76.2x152.4mm specimens so the results were comparable to the CFFT displacement-controlled load-strain test data.

2.4 Test Setup and Instrumentation

Displacement-controlled testing was executed for all CFFT specimens (i.e., both LWA and ND) to measure the applied axial compressive load vs. displacement, at a constant load rate of 2.5mm/min. These tests were carried out using a 2 MN Instron Hydraulic Universal Testing System (5590-HVL Series) to the point of ultimate failure, as shown in Fig. 2. Two axial and two lateral linear potentiometers (LPs) were used to measure the gradual displacement in contrast to the applied load in both the axial and lateral directions, respectively, for all unconfined concrete specimens and CFFTs. The LPs were set-up on opposing sides of each specimen (i.e., two axial LPs at 180° along the specimen circumference, and two lateral LPs at 90° to the axial LPs), as shown in Figure 3.

The axial and lateral LPs were connected to the CFFTs and unconfined concrete specimens using two aluminum yokes on both ends of the cylindrical specimens, where both yokes were connected by three fixed steel rods to facilitate the fitting process. Both aluminum yokes were rigidly connected to the outer surface of the specimens with three evenly separated bolts around the perimeter to prevent pivoting as shown in Figure 2b and Figure 3. Due to their accuracy, strain

gauges were attached to the CFFT specimens prior to testing to correlate the measured LP displacement data. The strain gauges were attached to the exterior surface of the CFFTs to measure the axial, hoop, and shear deformation, where they were specifically configured 0°, 90°, and 45°, respectively, to the loading plane.

3 ANALYTICAL STUDY

3.1 Classical Lamination Theory

Classical lamination theory (CLT) is used to consider the behavior of a thin GFRP laminate subjected to multiaxial loading. In this theory, the laminate is assumed to be a function of the properties of each individual layer that makes up the stacking sequence of the laminate. Per Daniel and Ishai [25], the individual lamina layers are assumed to be in a state of plane stress within the x-y plane (i.e., $\sigma_z = \tau_{xz} = \tau_{yz} = 0$ and $\varepsilon_z = \gamma_{xz} = \gamma_{yz} = 0$).

For this experiment, the $\pm 55°$ filament-wound GFRP tubes were fabricated so the orientation is symmetric about the middle through-thickness reference plane at coordinate 0. Therefore, it is assumed that there is strain compatibility between the measured strain of the laminate and all individual lamina layers in the stacking sequence (i.e., $[\varepsilon]_{xy} = [\varepsilon^0]_{xy}$). The material properties of the 1-2 plane, detailed in Table 1, are used to construct the stiffness matrix. The relationship can be transformed to an arbitrary plane (i.e., x-θ) using the transformation matrix in $[T]_{mn}$. This process is described by Eq. 2, as well as in further detail per Daniel and Ishai [25].

$$\begin{bmatrix}\sigma_x\\ \sigma_\theta\\ \tau_s\end{bmatrix}_k = \left[T^{-1}\right]_{mn} \begin{bmatrix} \frac{1}{E_1} & -\frac{\nu_{21}}{E_2} & 0 \\ -\frac{\nu_{12}}{E_1} & \frac{1}{E_2} & 0 \\ 0 & 0 & \frac{1}{2G_{12}} \end{bmatrix}_k^{-1} [T]_{mn} \begin{bmatrix}\varepsilon_x^0\\ \varepsilon_\theta^0\\ \frac{1}{2}\gamma_s^0\end{bmatrix}_k = \begin{bmatrix} Q_{xx} & Q_{x\theta} & 2Q_{xs} \\ Q_{\theta x} & Q_{\theta\theta} & 2Q_{\theta s} \\ Q_{sx} & Q_{s\theta} & 2Q_{ss} \end{bmatrix}_k \begin{bmatrix}\varepsilon_x^0\\ \varepsilon_\theta^0\\ \frac{1}{2}\gamma_s^0\end{bmatrix}_k \quad (2)$$

This expression can be modified to represent a resulting force per unit length that acts along the middle through-thickness reference plane. This accounts for the contribution of all lamina layers, representing a particular lamina layer, k, to a radial distance, z, from the middle through-thickness reference plane [25], shown in Eq. 3.

$$\begin{bmatrix} F_x \\ F_\theta \\ F_s \end{bmatrix} = \sum_{k=i}^{n} \left\{ \begin{bmatrix} Q_{xx} & Q_{x\theta} & Q_{xs} \\ Q_{\theta x} & Q_{\theta\theta} & Q_{\theta s} \\ Q_{sx} & Q_{s\theta} & Q_{ss} \end{bmatrix}_k \int_{z_{k-1}}^{z_k} dz \right\} \begin{bmatrix} \varepsilon_x^0 \\ \varepsilon_\theta^0 \\ \gamma_s^0 \end{bmatrix} \tag{3}$$

3.2 Biaxial loading behavior of composite material

The model presented by Jones and Nelson [15] was originally developed to describe the softening behavior associated with transversely isotropic composite material that's characterized by a nonlinear stress-strain response upon subjection to external mechanical loading. The composite in consideration is initially subjected to a simple uniaxial stress state to determine the nonlinear stress-strain relationship of each axis that is intended to be biaxially loaded (i.e., x-θ plane). Successive stress-strain values to the point of ultimate failure are then compared to their respective secant material properties (i.e., $E_{x,sec}$, $E_{\theta,sec}$, $v_{x\theta,sec}$**)** [15][25]. For a GFRP tube, this can be completed by bare tube axial compression testing, or hydraulic pressure testing for analyzing the tube's tensile hoop behavior. The successive material properties can then be described as a function of the equivalent linear complimentary strain energy density, U_i [15].

$$MP = A_i(1 - B_i U_i^{C_i}) \tag{4}$$

Coefficient A_i represents the initial linear-elastic material property, and coefficients B_i and C_i are determined by fitting Eq. 4 to the actual secant material property (MP) vs. strain energy density,

U_i, curve obtained experimental testing of the composite [15]. The equivalent linear complimentary strain energy density is expressed by Eq. 5 [15].

$$U_i = \frac{\sigma_x \varepsilon_x + \sigma_\theta \varepsilon_\theta + \tau_{x\theta} \gamma'_{x\theta}}{2} \quad (5)$$

After establishing the uniaxial MP vs. U_i curves, the nonlinear stress-strain behavior of a GFRP tube subjected to a biaxial state of stress may then be estimated by using both Eq. 4 and Eq. 5 in unison through an iterative process [15]. A modified version of Hooke's law compliance matrix discussed in Section 3.1 [25] for orthotropic material is employed to estimate the biaxial stress-strain relationship using secant values obtained from Eq. 6, in relation to a particular hoop strain interval. In this expression, it is assumed that there is no generation of out-of-plane shear stress or shear strain as the composite possesses radial symmetry about the central reference plane (i.e., no out-of-plane bending or displacement), as discussed in Section 3.1. It is also assumed that in-plane (x-θ) shear coupling is negligible for the P150 GFRP Tubes (thickness = 4.03), despite the x-θ plane being asymmetric. Theoretically, as the P150 GFRP tubes have an odd number of FRP layers within the laminate stacking sequence, and all layers consisting of fibers running at a $\pm 55°$ fiber orientation to the loading direction, compressive normal stresses subjected on the GFRP tube in the CFFT mechanism could create in-plane shear strains [25]. Due to the high degree of stiffness imposed on these GFRP tubes from the manufacturing process, along with symmetry about the through-thickness central refence plane, the tube itself would resist shear coupling effects making it difficult for it to arise. In-plane shear stress can also be neglected as it is assumed that the CFFTs are concentrically loaded under uniaxial compression (i.e., no twisting or applied bending moments). Accounting for all discussed assumptions, the GFRP tube's stiffness matrix may be

further simplified by removing properties related to shear stress and/or shear strain and is expressed via Eq. 6.

$$\begin{bmatrix}\varepsilon_x\\ \varepsilon_\theta\end{bmatrix}=\begin{bmatrix}S_{xx,sec} & S_{x\theta,sec}\\ S_{\theta x,sec} & S_{\theta\theta,sec}\end{bmatrix}\begin{bmatrix}\sigma_x\\ \sigma_\theta\end{bmatrix}=\begin{bmatrix}\frac{1}{E_{x,sec}} & \frac{v_{\theta x,sec}}{E_{\theta,sec}}\\ \frac{v_{x\theta,sec}}{E_{x,sec}} & \frac{1}{E_{\theta,sec}}\end{bmatrix}\begin{bmatrix}\sigma_x\\ \sigma_\theta\end{bmatrix} \quad (6)$$

For each iteration corresponding to a certain hoop strain value on the GFRP tube, the process is as follows [15]: (i) assume an initial axial strain corresponding to the hoop strain interval; (ii) assume initial material property values $E_{x,sec}$, $E_{\theta,sec}$, and $\nu_{x0,sec}$ by using linear-elastic properties if it is the first iteration, or the predicted secant material properties from the previous iteration of a particular hoop strain value for any other iteration; (iii) determine the biaxial stresses for the set of biaxial strain values using Eq. 6; (iv) calculate the biaxial linear equivalent value of U_i, from Eq. 5, using the set of current biaxial stresses and strains; (v) determine new secant material properties by inserting the calculated value of U_i from biaxial behavior into the determined uniaxial MP vs. U_i curves expressed by Eq. 4; (vi) continue this process with the initial set of axial and hoop strain values until there is negligible difference between the new and old complimentary strain energy density values. Xie et al. [6] suggests the tolerance between the new and old strain energy density values for a particular hoop strain interval be less than or equal to 10^{-6} expressed in Eq. 7. This procedure is continued for successively increasing hoop strain values until reaching the experimental hoop rupture strain value.

$$\Delta U_i=\frac{U_{i,new}-U_{i,old}}{U_{i,old}}\leq 10^{-6} \quad (7)$$

3.3 Confined strength of concrete prediction model

Popovics [26] originally proposed a model to estimate the stress strain response of unconfined concrete. Authors such as Jiang and Teng [16] modified this model to simulate the stress-strain

response of concrete confined with FRP, utilizing a successively increasing (variable) confinement pressure corresponding to an input hoop strain interval value. This model utilizes several elements to predict the stress-strain response of confined concrete, the first being a stress-strain relationship expressed by Eq. 8-10. The model originally proposed by Popovics [26] to estimate the unconfined concrete stress interval, $\sigma_{cc,i}$, is modified by implementing the peak FRP confined stress-strain values.

$$\sigma_{cc,i}=\frac{f'_{cc}xr}{r\text{-}1+x^{r}} \tag{8}$$

$$x=\frac{\varepsilon_{cc,i}}{\varepsilon'_{cc}} \tag{9}$$

$$r=\frac{E_c}{E_c\text{-}E'_{sec}} \tag{10}$$

The model includes: (i) A prediction of the peak axial strength of the confined concrete, f'_{cc}, per Eq. 11 [6], and the corresponding axial strain, ε'_{cc}, per Eq. 12 [6] for a specific interval, and is represented by the confined concrete secant modulus, E'_{sec}, within Eq. 10; (iii) An expression proposed by Teng et al. [27] to relate the axial strain-hoop strain of the FRP confined concrete, per Eq. 13; (iv) an expression describing the equilibrium between the variable confining pressure at GFRP tube-concrete core interface, $\sigma_{R,i}$, to the generated hoop stresses of the GFRP tube $\sigma_{\theta,i}$, per Eq. 14.

$$\frac{f'_{cc}}{f'_c}=1+3.3\frac{\sigma_{R,i}}{f'_c} \tag{11}$$

$$\frac{\varepsilon'_{cc}}{\varepsilon'_c}=1+17.5\left(\frac{\sigma_{R,i}}{f'_c}\right)^{1.2} \tag{12}$$

$$\frac{\varepsilon_{cc,i}}{\varepsilon'_c}=0.85\left[1+8\left(\frac{\sigma_{R,i}}{f'_c}\right)\right]\left\{\left[1+0.75\left(\frac{\varepsilon_{\theta,i}}{\varepsilon'_c}\right)\right]^{0.7}-exp\left[-7\left(\frac{\varepsilon_{\theta,i}}{\varepsilon'_c}\right)\right]\right\} \tag{13}$$

$$\sigma_{R,i}=\frac{2t\sigma_{\theta,i}}{D} \tag{14}$$

$$\sigma_{\theta,i} = Q_{\theta x}\, \varepsilon_{x,i} + Q_{\theta\theta,i}\, \varepsilon_{\theta} \quad (15)$$

Eq. 13 is built on the consensus that the bare GFRP tube and confined concrete core maintain the same axial strain under monotonically increasing compressive load [27]. The variable confining pressure, $\sigma_{R,i}$, can be obtained directly from the GFRP tube's generated hoop stress, $\sigma_{\theta,i}$, which corresponds to a particular hoop strain interval, $\varepsilon_{\theta,i}$, via Hooke's Law stiffness matrix for orthotropic material [25]. The model proposed by Jiang and Teng [26] was developed based on CFFTs composed of FRP tubes consisting of fibers aligned in the hoop direction. In this case, the effect of Poisson's ratio within the FRP tube was deemed negligible due to the lower degree of axial stiffness in the transverse direction in contrast to the hoop direction. The FRP tubes analyzed in the current research possess a considerable degree of stiffness in both the axial and hoop direction due to the $\pm 55^{o}$ fiber-winding angle. For this case, the effect of Poisson's ratio due to axial loading on the FRP tube within the CFFT mechanism must be considered when calculating the generated hoop stress increment, $\sigma_{\theta,i}$, in Eq. 15 to estimate the level of variable confinement pressure, $\sigma_{R,i,}$ as shown in Eq. 14. Subscript *i* denotes the i^{th} stress-strain interval.

3.4 Integrating Jiang and Teng's model [16] with Jones and Nelson's model [15]

In the present study, Jiang and Teng's model [16] describing the confined strength of concrete is incorporated into a Jones and Nelson's model [15], which predicts the stress-strain softening behavior of a specific composite material subjected to multiaxial loading. The process involves specifying an initial hoop strain interval value imposed on the CFFT and using the iterative model suggested by Xie et al. [6] to solve the CFFT's corresponding axial strain interval value, as well as the individual axial stress components subjected on the concrete core and the GFRP tube. The same process occurs for each individual hoop strain value specified at a particular interval (i.e., $\varepsilon_{h,i}$) between zero and the experimental hoop rupture strain value (i.e., $\varepsilon_{h,rup}$).

For a particular CFFT load-strain interval, the process consists of completing the following steps [6]: (i) Assume an initial axial strain value, $\varepsilon_{x,i}$, corresponding to the given hoop strain interval, $\varepsilon_{\theta,i}$; (ii) Verify the model proposed by Jones and Nelson [15] with satisfying the allowable tolerance (i.e., $\Delta U_i \leq 10^{-6}$ at $\varepsilon_{\theta,i}$) [6]; (iii) with the determination of $\sigma_{x,i}$ and $\sigma_{\theta,i}$, the confined strength of the concrete core, $\sigma_{c,i}$ and the corresponding axial strain $\varepsilon_{c,i}$ can be calculated using Eq's. 7 to 13 proposed by Jiang and Teng [16]; (iv) ensure that the axial strain imposed on the GFRP tube, $\varepsilon_{x,i}$, is within the allowable tolerance of $\leq 10^{-6}$ of the calculated axial strain of the confined concrete core, $\varepsilon_{c,i}$, as they are assumed to have the same degree of strain [6][9]; (v) if the tolerance is not satisfied, set $\varepsilon_{x,i}$ equal to $\varepsilon_{c,i}$, and reiterate for the current hoop strain interval from step (ii) until the allowable tolerance from step (iv) is satisfied (i.e., $\Delta\varepsilon \leq 10^{-6}$). Upon verifying all steps, calculate the axial compressive capacity on the CFFT, $P_{c,i,}$ from Eq. 16.

$$P_{c,i}=\sigma_{c,i}A_c+\left(-\sigma_{x,i}\right)A_{FRP} \tag{16}$$

This process is continued for successively increasing values of the hoop strain until the axial load capacity is determined at the experimental at the hoop rupture strain. This process is illustrated in using a flowchart shown in Figure 4 [6].

3.5 Obtaining the Material Property (MP) vs. U_i curve

To utilize Jones and Nelson's model [15], test data on the bare GFRP tubes are required. Betts et al. [12] tested both types of $\pm 55^{o}$ filament wound GFRP tubes (i.e., 50 PSI and 150 PSI) under pure compression to determine the axial stress-strain response. All tubes had a similar response under pure axial compression and mostly failed prematurely due to localized buckling. An average stress-strain response was developed from the data.

The bare GFRP tube stress-strain data presented in Figure 5 may be utilized directly to calculate the MP vs. U_i, curves. The initial tangent Poisson's ratio, $\nu_{x\theta,tan}^{i=0}$ represents the GFRP tube's

Poisson's ratio in the initial elastic range and was measured at approximately 0.34. From the data, there was only a slight degradation in the tangent Poisson's ratio with a reduction in its value. The $E_{x,sec}$ vs. U_x and $\nu_{x0,sec}$ vs U_x curves may be distinguished from Figure 5b [12]. Symmetry of the stiffness matrix (i.e., compatibility between $\nu_{x\theta}/E_x$ and $\nu_{\theta x}/E_\theta$) is assumed in the process [6][25].

To properly predict the nonlinear axial load-strain response of the CFFT under uniaxial compression, uniaxial tensile stress-strain data pertaining to the hoop direction of the GFRP tube is required to form the $E_{0,sec}$ vs. U_θ curve [6]. For the current research, there weren't enough sections of GFRP tubing to complete this testing; therefore, a uniaxial tensile stress-strain response regarding the GFRP tube's hoop direction was estimated. Subjecting the GFRP tube sections to internal pressure to ultimate failure by hoop rupture would have been an accurate method to obtain the uniaxial hoop tensile stress-strain data for these sections. The measured bare GFRP tube $E_{0,sec}$ vs. U_θ curve was approximated using linear interpolation between the tensile stress-strain test data at a $\pm 55^o$ fiber orientation to the loading axis, presented in Betts et al. [12], and the theoretical linear-elastic stress-strain response in the fiber direction using the elastic material properties to approximate the uniaxial tensile stress-strain curve of these bare GFRP tubes at a $\pm 35^o$ fiber orientation to the loading axis. The linear interpolation formula was set-up using the winding angle (e.g.., 0°, 35°, 55°) to approximate the measured bare GFRP tensile stress-strain curve to a strain value of 0.0225 mm/mm (i.e., the measured strain level at failure of uniaxial tensile testing of the bare GFRP tubes at $\pm 55^o$ winding angle to the loading plane). This data was then used to estimate the E_θ vs. U_θ curve as presented in Figure 6. This method of estimation is somewhat limited as it does not truly capture the actual uniaxial hoop tensile stress-strain response of the bare FRP tubes. The tensile hoop failure strain is set to a value of 0.0225 mm/mm in the linear interpolation formula, as it is bound to its axial failure strain from compression testing, as shown in Figure 5a

per Betts et al. [12]. To accurately capture the tensile stress-strain curve of these FRP tubes in the hoop direction, a form of uniaxial testing would need to be executed, such as open ended internal hydraulic pressure testing to failure [6].

3.6 Extrapolating of the Material Property (MP) vs. U_i curve

In most cases, the experimental strain energy density of the GFRP confining tube in a composite CFFT system will surpass the maximum strain energy density, U', determined from uniaxial compression testing of the bare GFRP tube, to a point of U_{max}. Xie et al. [6] suggests using a method originally proposed by Jones and Morgan [15] to extrapolate the MP vs. U_i curve passed U'. The authors suggest that as U_i approaches infinity, the secant value of the material property should asymptotically approach its tangent value measured at U', expressed by Eq. 17 [6][15].

$$MP_{sec} = \begin{cases} A_i(1\text{-}B_i U_i^{C_i}) & U_i \le U' \\ MP'_{tan} + \dfrac{a_i}{b_i + U_i} & U_i > U' \end{cases} \tag{17}$$

In Eq. (17), a_i and b_i are coefficients that are determined by allowing the extrapolated segment of the curve to smoothly connect to the first segment of the curve. Variable $MP'_{,tan}$ corresponds to the axial and hoop tangent moduli and minor tangent Poisson's ratio at U'. It was discovered that using this extrapolation method caused an over prediction of the axial capacity for a given value of strain in Jones and Nelson's [15] prediction model, mainly due to the underprediction in the degradation of the material's mechanical properties along both loaded axes at higher values of biaxial loading.

To account for this phenomenon, a new method is proposed to consider the higher degree of degradation in the material's mechanical properties, passed a point of U'. This method is only used to form the extrapolated region of the biaxial secant moduli (SM) MP vs. U_i curve, as the degradation of the Poisson's ratio is only minor. An additional constant is implemented to

characterize this enhanced degree of nonlinearity associated with the secant material properties of the biaxially loaded axes.

$$MP^{*}_{sec}=MP'_{tan}{}^{c_i}+\frac{a_i}{b_i+U_i} \qquad U_i > U' \tag{18}$$

$$c_i=1\text{-}d_i\left(\varepsilon^{*}_{i}\text{-}\varepsilon'\right) \tag{19}$$

where c_i, in Eq. 18, is a variable defined by constant di, which is determined in a similar fashion as constants a_i and b_i. This variable is used to simulate a value for tangent modulus at a particular strain interval value, ε^{*}_i, for U_i>U', based on the measured tangent moduli at U'. Constant d_i of Eq. 19 is axis dependent and will vary based on the type of loading and/or winding angle to the direction of imposed loading. Variable ε' is the strain measured at U'. As stated, the secant Poisson's ratio maintains an asymptotic approach towards the tangent Poisson's ratio determined at U' for U_i>U'; thus, ci is set equal to 1. Variable ci in Eq. 19 is further used as a factor to degrade the measured $MP'_{,tan}$ value from uniaxial testing of the bare GFRP tube specimens to represent an extrapolated tangent MP value at a strain interval exceeding ε'. Therefore, the value of constant d_i must implemented in Eq. 19 in such a way that it maintains a smooth transition into the extrapolated region of the MP vs. U_i curve as shown in Figure 6a for $E_{x,sec}$ vs. U_x.

It is assumed that the change in the tangent moduli, $\Delta E^{*}_{tan,(Umax\text{-}U')}$, within the extrapolated region of the uniaxial MP vs U_i curves between U_{max} and U', are negatively proportional to the change in the y-intercept stress value, $\Delta\sigma^{y}_{(Umax\text{-}U')}$, corresponding to the tangent moduli slope at U', and theoretically at U_{max} on an extrapolated version of the generated uniaxial stress-strain test data on the bare GFRP tube, shown in Eq 18.

$$-\Delta E^{*}_{tan,(U_{max}\text{-}U')} = \Delta\sigma^{y}_{(U_{max}\text{-}U')} \tag{20}$$

$$\Delta E^{*}_{tan,\,(U_{max}\text{-}U')}=E^{*}_{tan,\,U_{max}}\text{-}E^{*}_{tan,\,U'} \tag{21}$$

$$\Delta\sigma^{y}{}_{(U_{max}\text{-}U')}=\sigma^{y}_{U_{max}}\text{-}\sigma^{y}_{U'} \tag{22}$$

where, $E^*_{tan,U'}$, is the tangent moduli measured at U', and σ^y_U corresponds to the y-intercept stress value from the slope of $E^*_{tan,U'}$. The value for $\Delta E^*_{tan,(Umax-U')}$ is obtained through Eq. 21, by determining a value for tangent modulus, $E^*_{tan,Umax}$, at U_{max} using Eq. 18 for an adopted value of constant d_i and the ultimate experimental strain, ε_{max}, for a particular loaded axis. All intermediate values of tangent moduli, $E^*_{i,\,tan}$, for a particular value of strain, ε^*_i, between U' and U_{max}, may also be determined directly from Eq. 18. With the determination of $\Delta E^*_{tan,(Umax-U')}$, the value of $\Delta\sigma^y_{(Umax-U')}$ may be determined using Eq. 20. The measurable y-intercept stress value, $\sigma^y_{U'}$ at U', and the determined value of $\Delta\sigma^y_{(Umax-U'),}$ can be used in Eq. 22 to determine the theoretical y-intercept stress value, σ^y_{Umax}. An intermediate y-intercept stress value, $\sigma^*_{y,i}$, corresponding to $E^*_{i,\,tan}$ can be obtained using linear interpolation method expressed by Eq. 23.

$$\sigma^*_{y,i}=\frac{\sigma^y_{Umax}-\sigma^y_{U'}}{E^*_{tan,\,U_{max}}-E^*_{tan,\,U'}}\left(E^*_{i,tan}-E^*_{tan,\,U'}\right)+\sigma^y_{U'} \tag{23}$$

Obtaining values of $\sigma^*_{y,i}$ from Eq. 23 and $E^*_{i,\,tan}$ from Eq. 18 that correspond to a sequence of individual strain values, ε^*_i, between U' and U_{max}, (i.e., extrapolated region of the MP vs. U_i curve) a linear function may be implemented to evaluate the stress, σ^*_i that corresponds to a particular strain interval expressed by Eq. 24.

$$\sigma^*_i=E^*_{i,tan}\varepsilon^*_i+\sigma^*_{y,i} \tag{24}$$

With this data, intermediate values of the linear complimentary strain energy density, U^*_i, between U' and U_{max} may be determined by substituting the corresponding values of σ^*i and ε^*_i in Eq. 6. This process is followed to construct the extrapolated region of the uniaxial MP vs. U_i curves for each individually loaded axis of the GFRP tube in a gradual uniaxially compressed CFFT specimen to estimate the nonlinear biaxial loading behavior of the GFRP tube in a CFFT mechanism, as discussed in Section 3.2. Table 3 lists the determined constants in the current

research, as well as all evaluated MP'_{tan} and U' values corresponding to ε' from the bare GFRP tube test data. This method is graphically depicted in Figure 6b at various strain intervals equal to or above ε' (i.e., 0.0225mm/mm in this case) for the extrapolation of the $E_{x,sec}$ vs. U_x curve, as well as the extrapolation of the bare GFRP tube stress-strain response, shown in Figure 6a if required.

Using the following information, a graphical representation of model is illustrated in Figure 7 for the NDCFFT-P150 specimens at a hoop strain interval of -0.05 mm/mm. Inputting this value in the iterative load-strain prediction model presented by the flow chart shown in Figure 4, the CFFT axial strain increment, as well as the subjected axial compressive load increment to generate the biaxial deformation may be estimated. In this model, both the concrete core and GFRP tube are assumed to deform axially by the same amount under gradual displacement-controlled compressive loading. This means that the axial contraction of the GFRP tube due to the effect of Poisson's ratio $\nu_{\theta x}$, which results from imposed hoop stress due to lateral dilation of the concrete core, is assumed to be less than the imposed axial strain on the CFFT from uniaxial compressive loading at all strain intervals prior to failure [9].

4 RESULTS AND DISCUSSION

Displacement-controlled testing was executed for all unconfined concrete specimens and CFFT specimens to measure the applied axial load vs. biaxial displacement, at a constant load rate of 2.5mm/min. The test data collected from the axial LPs was analyzed and averaged to determine the mean incremental axial compressive strain, and the data collected by the lateral LPs was summed to determine the incremental hoop tensile strain. This data was then used to formulate the axial compressive load-axial strain response, as well as applied axial load-lateral strain response. The experimental incremental load-strain output to the point of ultimate failure may be observed

in Figure 8, where LWA concrete and ND concrete specimens of similar type are compared graphically. All strain gauges prematurely failed at an approximate value of 0.06 mm/mm; however, the strain gauge output data had sufficient correlation to the axial and lateral LP displacement measurements. It was also determined that there was a negligible degree of shear strain imposed on the CFFTs from the fixed 45° strain gauge during uniaxial compression loading of the specimens. This verifies the assumptions that were established to neglect in-plane shear stress and shear strain when constructing the FRP tube's stiffness matrix to predict the nonlinear axial compressive CFFT load-strain response in Section 3.1 and Section 3.2 [25]. This also indicates that the CFFTs, as well as the unconfined concrete cylinders, were purely loaded under uniaxial compression, and no twisting or imposed bending moments were subjected on the specimens during the displacement-controlled loading process.

The average peak measured values and deviations corresponding to the measured hoop rupture strain are listed in Table 4 and Table 5 for ND concrete specimens and LWA concrete specimens, respectively. A built-in iterative solver program in Microsoft Excel was used for prediction analysis of the CFFT's axial load-axial strain and axial load-hoop strain response. The solver was programed to follow the input-output model requirements illustrated in Figure 4. The initial measurable MP vs. U_i curves were determined using the coefficient of determination function, R^2, to mitigate variability between Eq. 5 and the independent bare GFRP tube's measured relationship.

In Phase 1 of the batching process, the unconfined concrete cylinders were subjected to load-controlled compression testing at 0.35 MPa/sec to determine the average compressive strength of both the LWA and ND concrete specimens. From this, it was determined that the LWA concrete specimens were represented by a smooth fracture plane upon failure, which can be observed in Figure 1b. These specimens were also met with a rapid decay of the axial stress-strain curve after

reaching its post peak compressive strength, noted by displacement-controlled testing in Phase 2 of the research. This was opposite to the ND concrete specimens from load-controlled testing in Phase 1, which were represented by a rough fracture plane upon compression failure as observed in Figure 1a. Phase 2 of the research also shows a post peak gradual decay of the stress-strain curve for the unconfined ND concrete specimens from displacement-controlled compression testing. A comparison of the axial stress-strain response is made in Figure 8a between both ND and LWA concrete specimens to visually show the brittle nature of LWA concrete from compression failure. The determined failure mode uniaxial compression for both types of concrete was expected following the theory of concrete compression failure as outlined per Bogas and Gomes [17] in Section 1.

From visual interpretation, there is a considerable increase in strength and ductility for both types of NDCFFTs and LWACFFTs (i.e. P50 and P150 CFFT types). Both P50 and P150 NDCFFTs obtained, on average, a higher peak bearing capacity than the LWACFFTs of the same classification as the ND concrete cores had a higher average peak compressive strength than the LWA concrete cores. However, the P50 and P150 LWACFFTs delivered a similar degree of enhanced strength and ductility in contrast to the NDCFFTs, which can be observed in Table 4 and 5. Also, the GFRP tubes assisted in eliminating the brittleness associated with unconfined LWA concrete prior to failure under compressive loading. Therefore, it can be stated that the LWACFFTs in this study have shown great potential in being implemented as a structural bearing component with the presence of the $\pm 55^{o}$ filament-wound GFRP tube(s). During the concrete batching process, it was determined that the hardened density of LWA concrete was 492 kg/m^3 lower than the ND concrete. This shows the capability LWACFFTs have in potentially reducing dead loads, project costs, and structural materials in heavy civil construction projects. Regarding

the experimental results presented in Figure 8a-c, it can be noted that with a lower D/t ratio, there seems to be a substantial increase in both strength and ductility (i.e., between the P50-CFFTs and the P150-CFFTs) as the thick-walled GFRP tubes can sustain a higher degree of internal pressure. Also, per Hain et al. [9], this indicates that a multidirectional fiber winding angle of $\pm 55°$ is sufficient for providing a certain degree of concrete core confinement. Based on the findings of Hain et al. [9], if the FRP tube's Poisson's ratio, $\nu_{x\theta}$, in reference to the axial loading direction is greater than 0.45 (i.e., Poisson's ratio of cracked concrete), increasing the number of filament-wound FRP layers, which reduces the D/t ratio, is ineffective at providing concrete confinement. This would result in minimal difference between the CFFT and unconfined concrete load-strain response. In conclusion on this topic, increasing the thickness of the FRP tube in a CFFT cannot make up for an insufficient fiber orientation, in this case less than $\pm 51.5°$ [7][9].

All CFFT specimens were characterized by an instantaneous failure by FRP hoop rupture along the full length of the CFFT's exterior surface in the axial direction as shown in Figure 2c-d. Upon further inspection of the failed specimens after removal from the testing apparatus, it was determined that the rupture location occurred at both LP yoke fixture points along the CFFT's exterior surface. As the CFFT specimens began to deform laterally as a consequence of uniaxial compression, the bolts used as the rigid fixture began penetrating the CFFT in the radial direction. This most likely initiated failure of the CFFTs by creating localized stiffness degradation; thus, indicating that the CFFTs failed prematurely. For future displacement-controlled testing using an LP apparatus of this type, the authors suggest using an impenetrable barrier between the fixture and the exterior surface of the CFFT to mitigate damage to the specimens during testing.

The prediction of the axial compressive behavior for both NDCFFT-P50 and NDCFFT-P150 seems to have sufficient correlation to the experimental axial load-biaxial (i.e., axial and hoop

direction) strain results. For both NDCFFT-P50 and NDCFFT-P150 CFFT specimens, a comparison between the model and experimental results are illustrated in Figure 9a and Figure 9b respectively. The experimental hoop rupture strain was measured on average at -0.066 mm/mm for the NDCFFT-P50 specimens and at -0.088 mm/mm for the NDCFFT-P150 specimens as shown in Table 4. These values were determined from the CFFT compressive test results, and used as the hoop rupture strain, $\varepsilon_{h,rup}$, in the CFFT load strain prediction model. Observing Figure 10a-b, the experimental axial load-strain response of the all LWACFFT-P50 and LWACFFT-P150 specimens also have sufficient correlation to the prediction model. The experimental hoop rupture strain was measured on average at -0.063 mm/mm for the LWACFFT-P50 specimens and at -0.095 mm/mm for the LWACFFT-P150 specimens as shown in Table 5.

Regarding the NDCFFT-P50 and LWACFFT-P50 specimens, the model has noticeable variability in the earlier stages of axial loading, specifically prior to reaching an axial/hoop strain value of 0.02 mm/mm. Xie et al.'s prediction model [6] in this region underestimates the applied axial load on the CFFT which may be attributed to the structural instability of the bare GFRP tubes during compression testing per Betts et al. [12]. Due to the gradual type of premature localized buckling failure imposed on the bare GFRP tubes during testing as shown in Figure 5a [12], the measured stress-strain response exhibits an under estimation of the relationship. This associates the GFRP tube as having higher degree of strain softening behavior than what actually would occur, as it's constrained from developing areas of localized buckling from lateral support by the concrete core [9][12].

For the NDCFFT-P150 and LWACFFT-P150 specimens, it is apparent that there is a notable degree of variability between the prediction model and experimental compressive behavior following an imposed axial and hoop strain of 0.02 mm/mm. From the results shown in Figure 8c,

the constant load rate of 2.5 mm/min could have possibly been too slow as both types of P150-CFFT specimens experienced a strain hardening region within their load-strain response. In the first portion of the load-strain response, the CFFT seems to decay at lower applied loads than anticipated (i.e., in comparison to the prediction model) as the low loading rate may result in reduced strength since generated cracks have more time to propagate through the concrete core, similar to the mechanism of creep [28]. This phenomenon is more recognizable in the LWACFFTs constructed with P150 GFRP tubes from Figure 10b, which is understandable as the LWA concrete core is significantly more brittle than the ND concrete core, as shown in Figure 8a. The experimental load-strain response of all P150-CFFT specimens is further characterized by a strain hardening region prior to ultimate failure. This theoretically may occur as the GFRP tube becomes activated at a relatively low applied load due to the slow loading rate. The immense stiffness possessed by the P150 GFRP tubes allows for an increased load-strain reaction, where a higher degree of applied energy is required to further degrade the GFRP tubes to the point of failure. As the P150 tubes are activated at a relatively low compressive load, more applied energy to the P150-CFFT specimens will be required to further enhance crack propagation through the GFRP tube. This is especially the case at material grain boundaries, where stress build-up in the material is required to increase dislocation points and further enable deformation to adjacent material grains, recognized as Frank-Read sources [28][29]. As the P50 GFRP tubes are less stiff than the P150 GFRP tubes, this strain hardening response is less recognizable at a displacement rate of 2.5mm/min because less energy is required to promote cracking or material dislocations across grain boundaries to an adjacent material grain [29].

From the modified version of Xie et al.'s [6] iterative model, it is predicted that the FRP tube will resist a considerable portion of axial compressive forces as a component of the CFFT

mechanism. This transpires as the FRP tube has a recognizable degree of stiffness in the axial direction, which was estimated by the CLT method and illustrated by the results of uniaxial compression testing of the $\pm 55°$ filament-wound FRP tubes utilized in this research, as shown in Figure 5 [12][25]. Figure 11 displays the contribution each component of the CFFT provides in resisting applied axial compressive loading for both the NDCFFT-P50 and NDCFFT-P150 specimens, as predicted by the Xie et al.'s [6] modified prediction model. It is clear from Figure 11 that the thicker P150 FRP tubes contribute to the CFFT's bearing capacity more than the P50 FRP tubes, as expected. This occurs as the P150 FRP tubes have approximately two times the surface area of the P50 FRP tubes and are significantly stiffer in the axial direction, as shown from the product of the CLT method by Eq. 3 [25]. It can be observed that the iterative model predicts a slight strain softening region at an axial strain of 0.0225 mm/mm (i.e., at U'). This occurs as Jones and Nelson's model [15] perceives the FRP tubes as having a great degree of strain softening behavior from the imposition of the bare tube compression data per Betts et al. [12]. In reality, the FRP tube in a CFFT mechanism is restrained from experiencing areas of localized buckling and is categorized by a smooth monotonically ascending load-strain response, as shown in Figure 8. If FRP composites can be restrained from premature failure when conducting uniaxial testing, a smoother transition point will be imposed on Xie et al.'s [6] extrapolation function for Jones and Nelson's model [15], as described by Eq. 18. This will mitigate the small area of predicted strain softening behavior shown in Figure 11 (i.e., at U') and will provide a more accurate representation of the actual load-strain behavior of CFFTs.

5 FUTURE RESEARCH

This research should be expanded by fabricating additional specimens with larger tube diameters to thoroughly evaluate the effect of size on the deformability of filament-wound GFRP tubes filled

with lightweight aggregate concrete. Testing a broader range of specimens will provide valuable insights into how increasing the diameter influences the structural performance and failure modes of the system under various loading conditions. Additionally, further testing should include specimens with varying concrete densities and strengths. This will enable a comprehensive assessment of how different material properties affect the overall behavior of the CFFT system, potentially identifying optimal combinations that enhance performance in practical applications. Furthermore, the analytical model should be expanded to predict the ultimate strain of the specimens. The main limitation of the analytical model is its calibration of the biaxial softening behavior based on the strain energy density of ±55^{o} tubes. Therefore, the model should be further verified against new test data from CFFTs made with angle-ply tubes featuring fiber orientations other than ±55^{o}.

6 CONCLUSIONS

In the current research, a total of 16 filament wound CFFTs were fabricated to measure the axial load-strain response. This included the production of five P50-LWACFFTs, five P150-LWACFFTs, five P50-NDCFFTs, and five P150-NDCFFTs, where the P50 GFRP tubes have a thickness of 1.87 mm (thin-walled) and the P150 GFRP tubes have a thickness of 4.03 mm (thick-walled). The CFFT's experimental axial load-strain response is compared to their unconfined counterpart under displacement-controlled testing at 2.5mm/min. This was conducted to determine the potential in using LWA concrete as a structural component, as it was determined in this study that the unconfined LWA concrete specimens were brittle in nature, characterized by a rapid decay of the axial stress-strain curve after reaching its post peak compressive strength. The addition of the exterior GFRP tube in the CFFT mechanism significantly enhanced both compressive strength and ductility of both ND and LWA unconfined concrete specimens. This paper presented a

modified version of Xie et al.'s prediction model [6] to estimate the theoretical axial load-strain response of a CFFT subjected to uniaxial compression. A modification factor was added to the iterative process within the MP vs. Ui curve's extrapolated region. This method was utilized to capture the enhanced nonlinear biaxial behavior associated with CFFTs composed of off-axis filament wound GFRP tubes. A comparison was made between the modified prediction model and the experimental load-strain response regarding its accuracy in predicting the uniaxial compressive behavior of CFFTs characterized by a $\pm 55^{o}$ fiber orientation. The following conclusions can be drawn:

- The GFRP tube's mechanical properties and fiber winding angle of $\pm 55^{o}$ permitted sufficient concrete core confinement. This is highlighted by a significant degree of compressive strength enhancement for all CFFTs in contrast to the unconfined specimens.
- In comparison with unconfined concrete, the compressive strength of the NDCFFT-P50 and NDCFFT-P150 CFFTs increased, on average, by a factor of 2.25 and 4.09, respectively. On the other hand, the compressive strength of the LWACFFT-P50 and LWACFFT-P150 CFFTs increased, on average, by a factor of 2.13 and 4.87, respectively.
- Increasing the GFRP tube thickness (i.e., reduction in the GFRP tube's D/t ratio) caused an increase in the axial capacity for both ND and LWA CFFTs. This concludes that these tubes will provide an effective degree of confinement with a multidirectional winding angle of $\pm 55°$.
- The implementation of the modified extrapolation factor for the MP vs. Ui curve's aided in capturing the higher degree of nonlinearity associated in the CFFT's axial compressive behavior for off-axis filament wound GFRP tubes.

- Xie et al.'s [6] modified prediction model suggests the ±55° filament-wound FRP tube will contribute 16% and 32% of the total bearing capacity within the NDCFFT-P50 and NDCFFT-P150 specimens, respectively, at the point of ultimate failure. This model also predicts that these FRP tubes will contribute approximately 15% and 37% of total bearing capacity in the LWACFFT-P50 and LWACFFT-P150 specimens, at the point of failure.
- From Xie et al's [6] modified load-strain prediction model, it is estimated that the effect the ±55° filament-wound FRP tube in resisting axial compressive forces gradually increases and becomes more relevant as applied load increases. Theoretically, this is a sufficient approximation, as the concrete core would be subjected to extensive cracking and deform quite rapidly, where its axial resistance properties would continue to diminish with increased loading.
- All CFFTs had a similar degree of strength enhancement when compared to their unconfined counterparts, regardless of the concrete core aggregate type, strength, or density. Overall, given the brittle nature of unconfined LWA concrete, the results indicate that LWA concrete shows promise in CFFTs for producing structural elements with enhanced load-bearing capacity and flexibility.

7 DATA AVAILABILITY STATEMENT

The raw/processed data required to reproduce these findings cannot be shared at this time due to technical or time limitations

8 REFERENCES

[1] Fam AZ, Rizkalla SH. Flexural behavior of concrete-filled fiber-reinforced polymer circular tubes. Journal of composites for construction. 2002 May;6(2):123-32.

[2] Naguib W, Mirmiran A. Flexural creep tests and modeling of concrete-filled fiber reinforced polymer tubes. Journal of Composites for Construction. 2002 Nov;6(4):272-9.

[3] Sadeghian P, Lai YC, Fam A. Testing and modeling of a new moment connection of concrete-filled FRP tubes to footings under monotonic and cyclic loadings. Journal of Composites for Construction. 2011 Aug 1;15(4):653-62.

[4] Fam AZ, Rizkalla SH. Confinement model for axially loaded concrete confined by circular fiber-reinforced polymer tubes. Structural Journal. 2001 Jul 1;98(4):451-61.

[5] Sadeghian P, Fam A. A rational approach toward strain efficiency factor of fiber-reinforced polymer-wrapped concrete columns. ACI Structural Journal. 2014 Jan 1;111(1):135-44.

[6] Xie P, Lin G, Teng JG, Jiang T. Modelling of concrete-filled filament-wound FRP confining tubes considering nonlinear biaxial tube behavior. Engineering Structures. 2020 Sep 1;218:110762.

[7] Vincent T, Ozbakkaloglu T. Influence of fiber orientation and specimen end condition on axial compressive behavior of FRP-confined concrete. Construction and Building materials. 2013 Oct 1;47:814-26.

[8] Zhu Z, Ahmad I, Mirmiran A. Effect of column parameters on axial compression behavior of concrete-filled FRP tubes. Advances in Structural Engineering. 2005 Aug;8(4):443-9.

[9] Hain A, Motaref S, Zaghi AE. Influence of fiber orientation and shell thickness on the axial compressive behavior of concrete-filled fiber-reinforced polymer tubes. Construction and Building Materials. 2019 Sep 30;220:353-63.

[10] Lu C, St. Onge J, Fam A. Damage threshold of near-cross-ply tubes used in concrete-filled FRP tubes loaded in flexure. Journal of Composites for Construction. 2020 Apr 1;24(2):04019063.

[11] Betts D, Sadeghian P, Fam A. Investigation of the stress-strain constitutive behavior of ±55 filament wound GFRP pipes in compression and tension. Composites Part B: Engineering. 2019 Sep 1;172:243-52.

[12] Betts D, Sadeghian P, Fam A. Experimental and analytical investigations of the flexural behavior of hollow ±55 filament wound GFRP tubes. Thin-Walled Structures. 2021 Feb 1;159:107246.

[13] Jawdhari A, Fam A, Sadeghian P. How Concrete Filling Fundamentally Changes Stress–Strain Curve of Angle-Ply FRP Tubes in Tension. Journal of Composites for Construction. 2022 Oct 1;26(5):04022063.

[14] Hahn HT, Tsai SW. Nonlinear elastic behavior of unidirectional composite laminae. Journal of Composite Materials. 1973 Jan;7(1):102-18.

[15] Jones RM, Nelson Jr DA. A new material model for the nonlinear biaxial behavior of ATJ-S graphite. Journal of Composite Materials. 1975 Jan;9(1):10-27.

[16] Jiang T, Teng JG. Analysis-oriented stress–strain models for FRP–confined concrete. Engineering Structures. 2007 Nov 1;29(11):2968-86.

[17] Bogas JA, Gomes A. Compressive behavior and failure modes of structural lightweight aggregate concrete–Characterization and strength prediction. Materials & Design. 2013 Apr 1;46:832-41.

[18] Cui HZ, Lo TY, Memon SA, Xu W. Effect of lightweight aggregates on the mechanical properties and brittleness of lightweight aggregate concrete. Construction and Building materials. 2012 Oct 1;35:149-58.

[19] Wei H, Wu T, Liu X, Zhang R. Investigation of stress-strain relationship for confined lightweight aggregate concrete. Construction and Building Materials. 2020 Sep 30;256:119432.

[20] J.G.M Van Mier, Fracture propagation in concrete under complex stresses, Fracture of Concrete and Rock: SEM-RILEM International Conference, Houston, TX, pp. 362-375, June, 1987.

[21] American Concrete Institute, "Selecting Proportions for Normal-Density and High-Density Concrete – Guide" ACI PRC 211.1-22, first ed., Detroit, United States of America: ACI Cmte, 2022.

[22] American Concrete Institute, "Standard Practice for Selecting Proportions for Structural Lightweight Concrete" ACI 211.2, first ed., Detroit, United States of America: ACI Cmte, 1998.

[23] American Concrete Institute, "Building [Code Requirements for Structural Concrete" ACI CODE 318-19, second ed., ACI Cmte 318 2022.

[24] Norlite LLC, "*Norlite Expanded Shale Aggregate*" Structural Concrete: Norlite. https://www.norliteagg.com/norlite

[25] Daniel IM, Ishai O. Engineering mechanics of composite materials. New York: Oxford university press; 2006.

[26] S. Popovics, "A numerical approach to the complete stress-strain curve of concrete" Cem Concr Res, vol. 3, no. 5, pp. 583-599, 1973.

[27] J.G. Teng, Y.L. Huang, L. Lam, L.P. Ye, "Theoretical Model for Fiber-Reinforced Polymer-Confined Concrete" J Compos Constr, vol. 11, no. 2, pp. 201-210, Sep, 2007, DOI: 10.1061/(ASCE)1090-0268(2007)11:2(201)

[28] A.I. Abdullah, “Effects of Loading Rate on Concrete Compressive Strength”, IOP Conf Ser: Mater Sci Eng, pp. 1-7, June, 2021, doi:10.1088/1757-899X/1144/1/012033

[29] J.W. Morris, “Dislocation-controlled Plasticity of Crystalline Materials: Overview”, Ency Mater: Sci Tech, second ed., pp. 2245-2255, 2001, https://doi.org/10.1016/B0-08-043152-6/00402-2

Table 1. Material properties.

GFRP Tube Properties: $V_f = 55\%$				
E_1 (MPa)	E_2 (MPa)	$v_{(12)}$	$v_{(21)}$	G_{12} (MPa)
41,000	10,400	0.28	0.06	4,300
ND Concrete Properties			**LWA Concrete Properties**	
f'_c (MPa)	E_c (MPa)		f'_c (MPa)	E_c (MPa)
31.2	27,757		24.7	18,870

Table 2. Test matrix

Group	Specimen ID	Quantity	FRP Layers	Height (mm)	Core Diameter (mm)	Wall Thickness (mm)	Layup Code (°)
ND-UC	UCND-28(S)	3	-	152.4	76.2	-	-
	UCND-28(L)	6	-	203.2	101.6	-	-
LWA-UC	UCLWA-28(S)	3	-	152.4	76.2	-	-
	UCLWA-28(L)	6	-	203.2	101.6	-	-
ND-C	NDCFFT-P50	4	4	159.9	76.2	1.87	$[\pm 55]_S$
	NDCFFT-P150	4	10	168.5	76.2	4.03	$[(\pm 55)_2/+55]s$
LWA-C	LWACFFT-P50	4	4	159.9	76.2	1.87	$[\pm 55]_S$
	LWACFFT-P150	4	10	168.5	76.2	4.03	$[(\pm 55)_2/+55]_S$

LWA=Lightweight Aggregate; ND=Normal Density; UC=Unconfined; C=Confined; P50 and P150 refers to the original pressure rating of the GFRP tube.

Table 3. Distinguished material properties and modified constants per Jones and Nelson's Model.

MP	MP'_{tan}	U'	A_i	B_i	C_i	a_i	b_i	d_i
$E_{x,sec}$	1898	1.34	10859	0.456	0.475	5200	0.250	0.300
$E_{\theta,sec}$	2732	1.79	18833	0.550	0.220	16740	2.08	0.250
$\nu_{x\theta,sec}$	0.243	1.34	0.375	0.149	0.454	0.549	6.71	N/A

Table 4: Experimental axial compressive behavior ND concrete specimens.

Specimen		Average Peak Values			Standard Deviation		
No.	Notation	Axial Strain	Hoop Strain	Force (kN)	Axial Strain	Hoop Strain	Force (kN)
1	UCND-28(S)	0.0021	-0.0013	143.9	2.1E-04	8.7E-04	2.01
2	NDCFFT-P50	0.084	-0.067	324.2	0.0095	0.0051	11.2
3	NDCFFT-P150	0.115	-0.088	589.2	0.0073	0.0053	10.3
4	Model: P50 (ND)	0.066	-0.067	301.1	0.018	0	23.1
5	Model: P150 (ND)	0.127	-0.088	571.5	0.012	0	17.5

Table 5: Experimental axial compressive behavior LWA concrete specimens.

Specimen		Average Peak Values			Standard Deviation		
No.	Notation	Axial Strain	Hoop Strain	Force (kN)	Axial Strain	Hoop Strain	Force (kN)
1	UCLWA-28(S)	0.003	-0.0006	111.1	8.5E-05	1.4E-04	5.39
2	LWACFFT-P50	0.066	-0.063	237.1	0.0042	0.0047	0.94
3	LWACFFT-P150	0.130	-0.095	541.1	0.0098	0.0032	12.9
4	Model: P50 (LWA)	0.067	-0.063	240.6	0.001	0	3.50
5	Model: P150 (LWA)	0.164	-0.095	549.0	0.043	0	7.90

Figure 1. fracture plane of the unconfined concrete specimens from load-controlled axial compression testing: a) normal density concrete cylinders and; b) lightweight aggregate concrete cylinders.

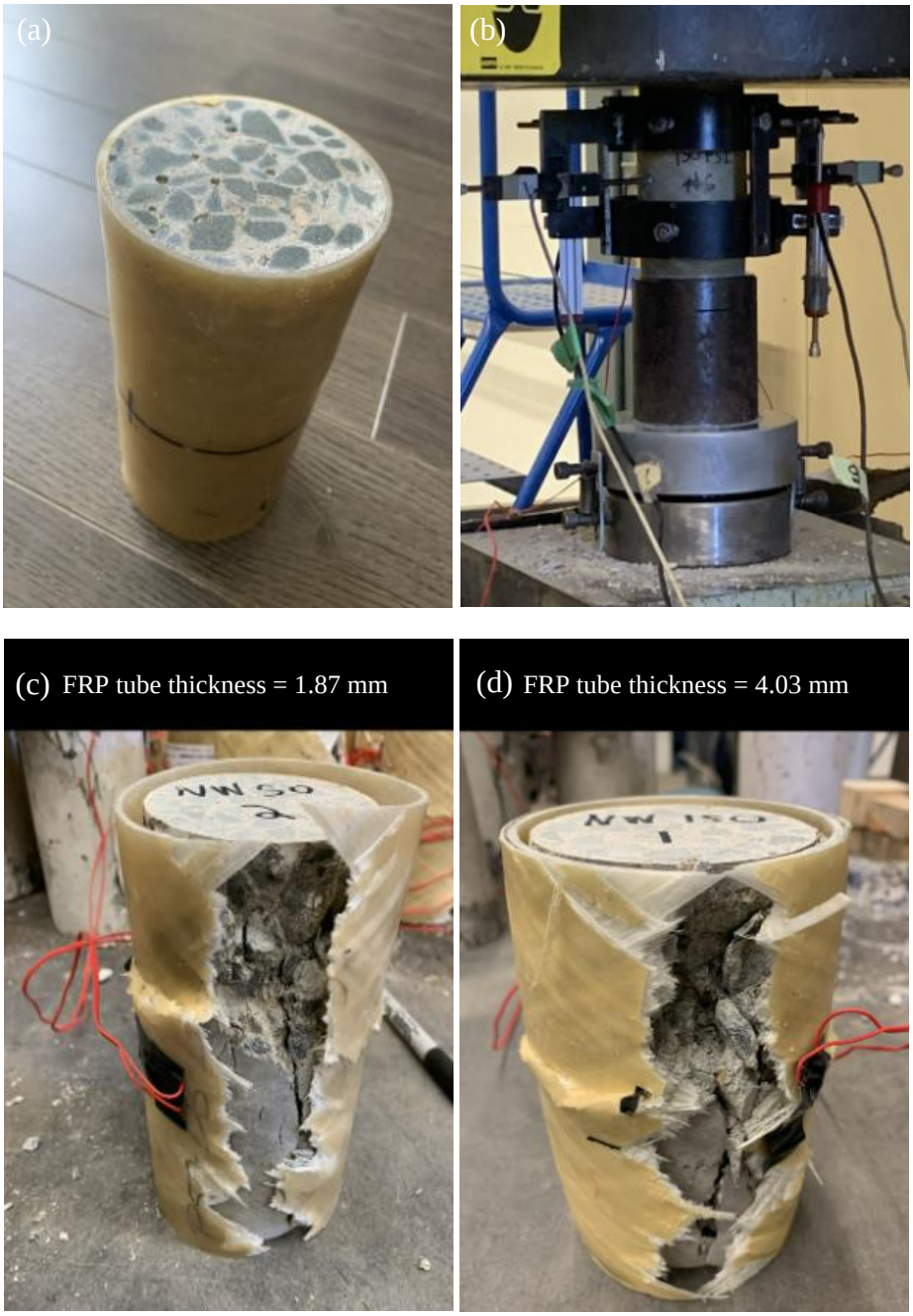

Figure 2. CFFT Test Specimens: a) NDCFFT-P150 test specimen end grinded at a 2:1 ratio; b) displacement-controlled testing of the CFFT specimens; c) P50-NDCFFT failure; d) NDCFFT-P150 hoop rupture failure.

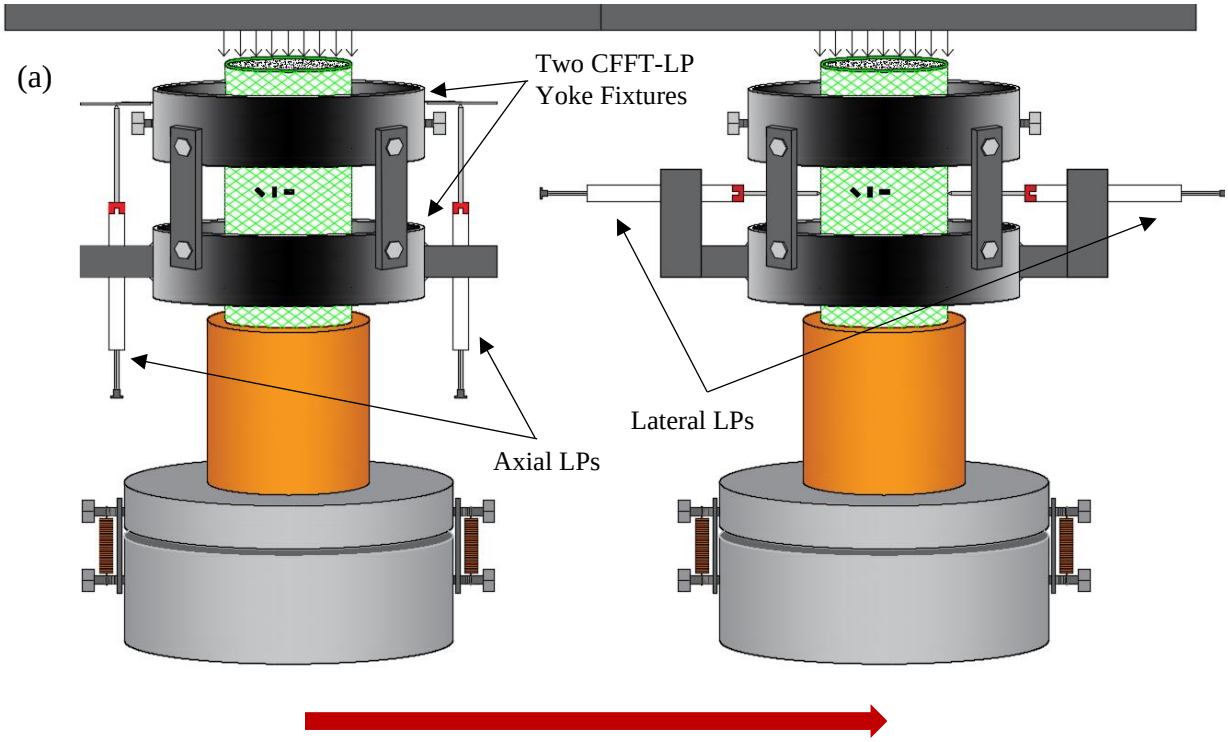

Figure 3. CFFT compression test set-up schematic: a) displacement-controlled compression test set-up at two different viewpoints; b) cross-section of CFFT strain gauge set-up; c) side view of CFFT with strain gauge set-up.

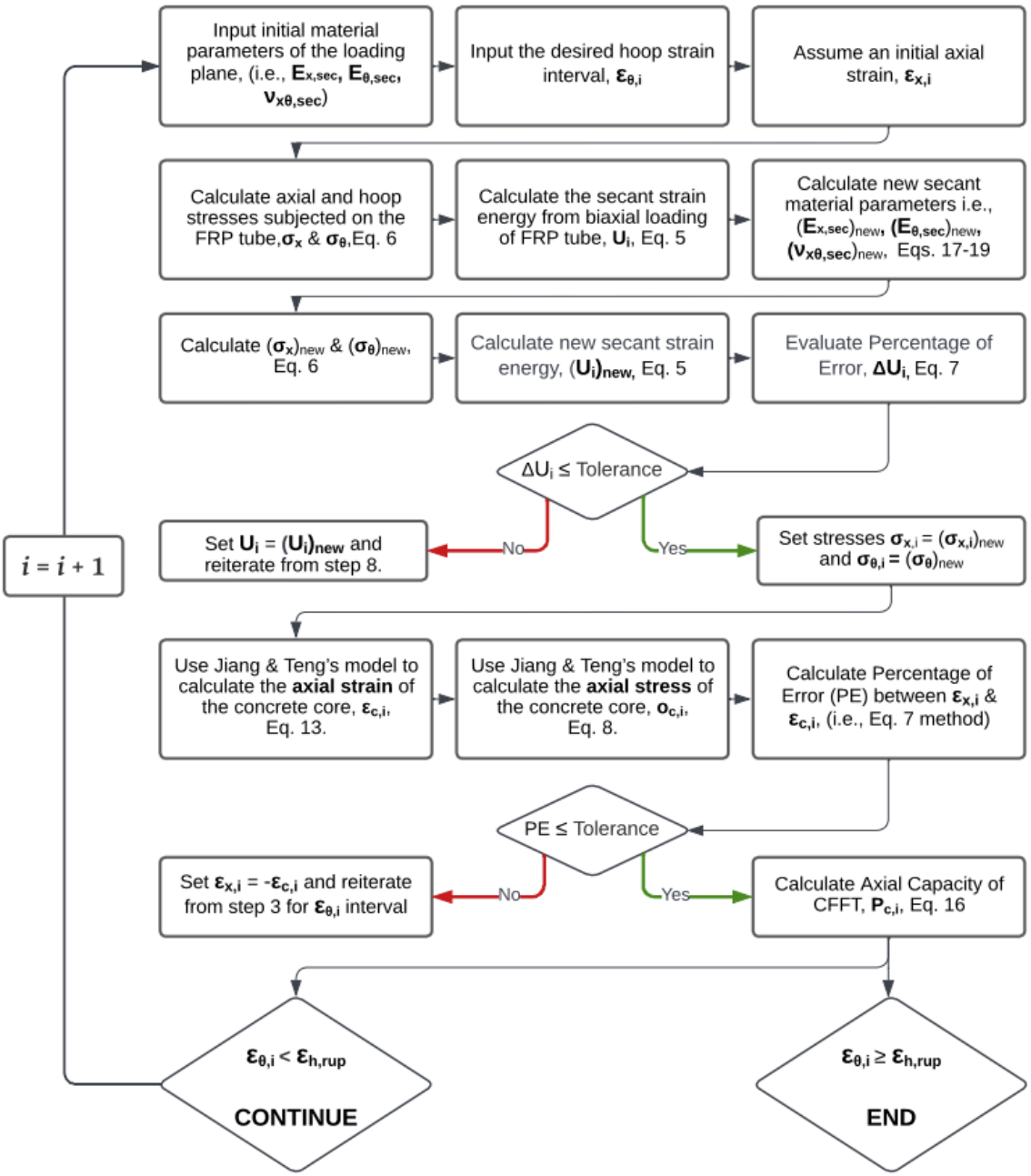

Figure 4. Flowchart of Xie et al.'s modified prediction model to determine the load-strain response for a CFFT under uniaxial compression.

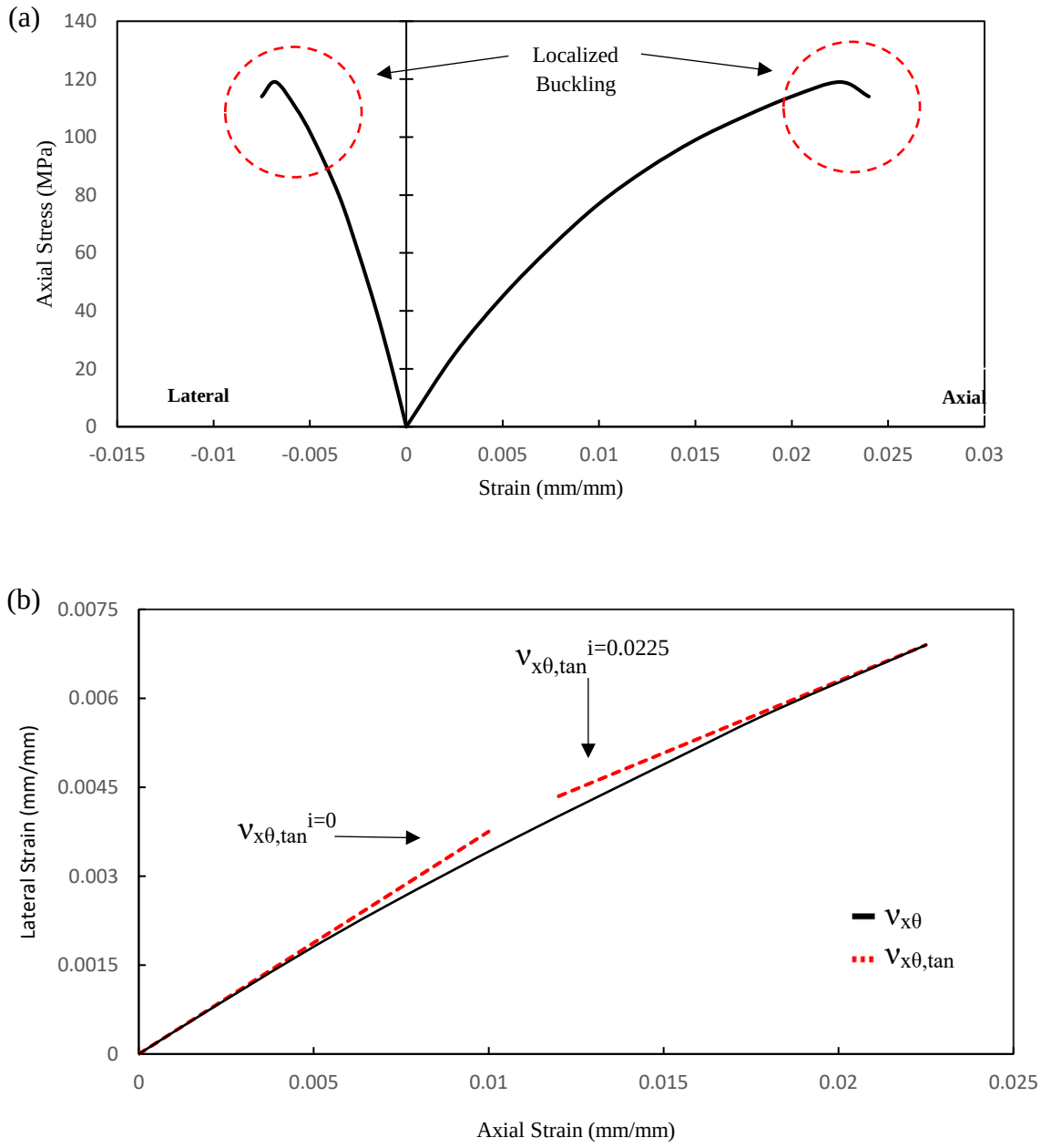

Figure 5. The nonlinear axial compressive behavior of the bare GFRP tubes: a) Average axial stress-strain response of 8 test results on the P50 and P150 GFRP tubes per Betts et al. [12]; b) Average incremental Poisson's Ratio showing Tangent Poisson's Ratio degradation with increased loading.

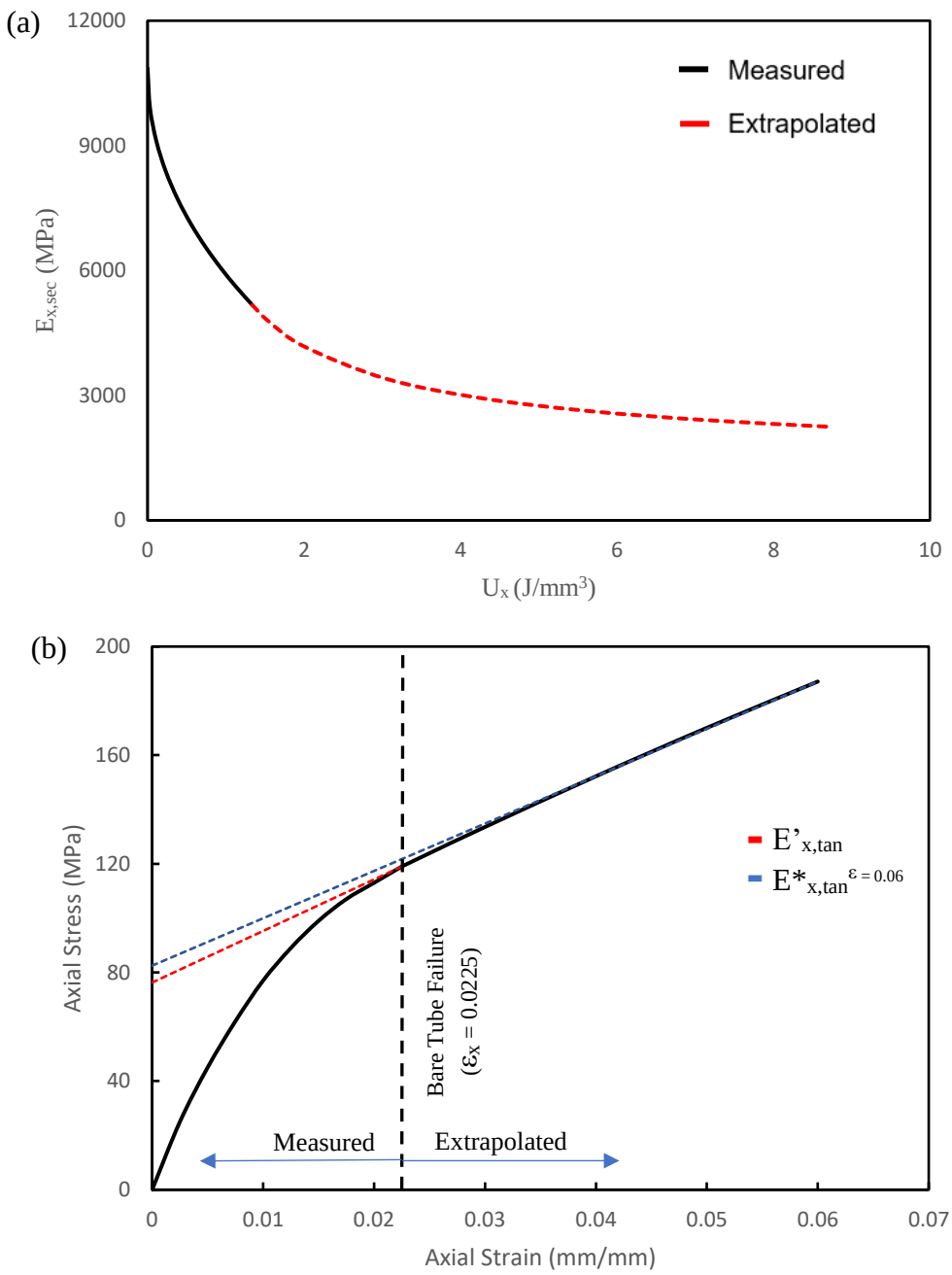

Figure 6. Extrapolation of the bare GFRP tube's axial stress-strain behavior using the modified method (Eq. 19) in Jones and Nelson's prediction model: a) Extrapolation of the $E_{x,sec}$-U_x curve; b) Determination of successive $E^*_{x,tan}$ and y-int* values (e.g., $E_{x,tan}$ and y-int. at ε=0.035) from $E'_{x,tan}$ in Eq. 19 to formulate extrapolation of the bare GFRP tube's axial stress-strain response as well as the extrapolation of $E_{x,sec}$ vs. U_x.

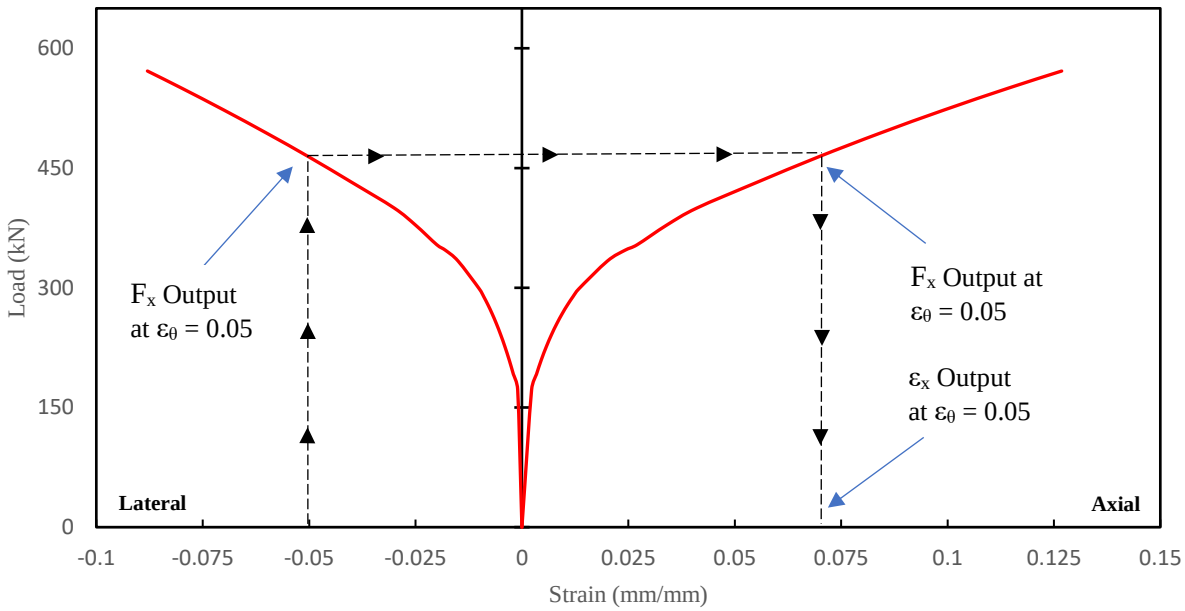

Figure 7. Model output depiction for a NDCFFT-P150 specimen at a hoop strain interval value of -0.05 mm/mm.

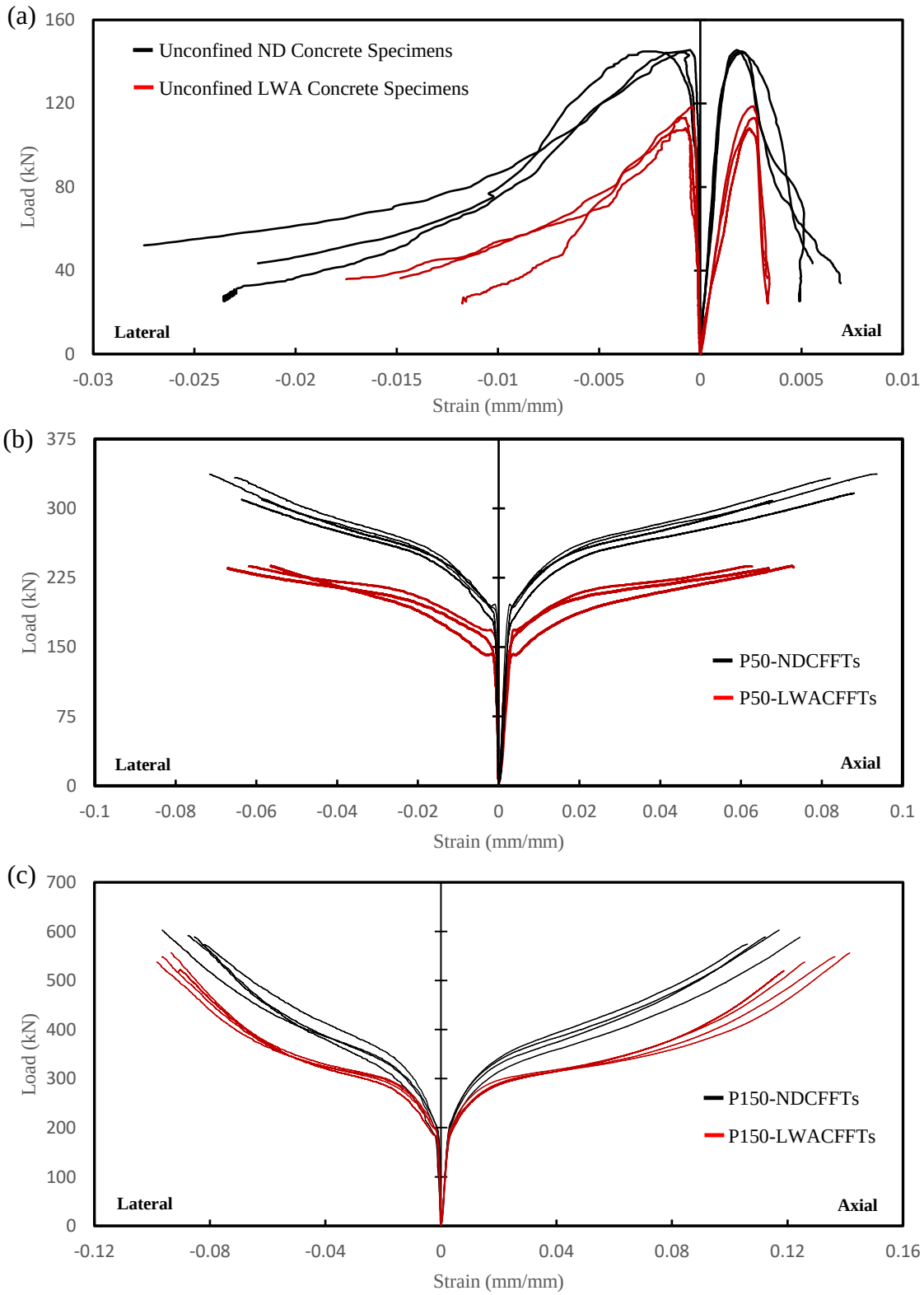

Figure 8. Displacement-controlled load-strain experimental results: a) unconfined concrete specimens; b) P50-CFFTs; c) P150-CFFTs.

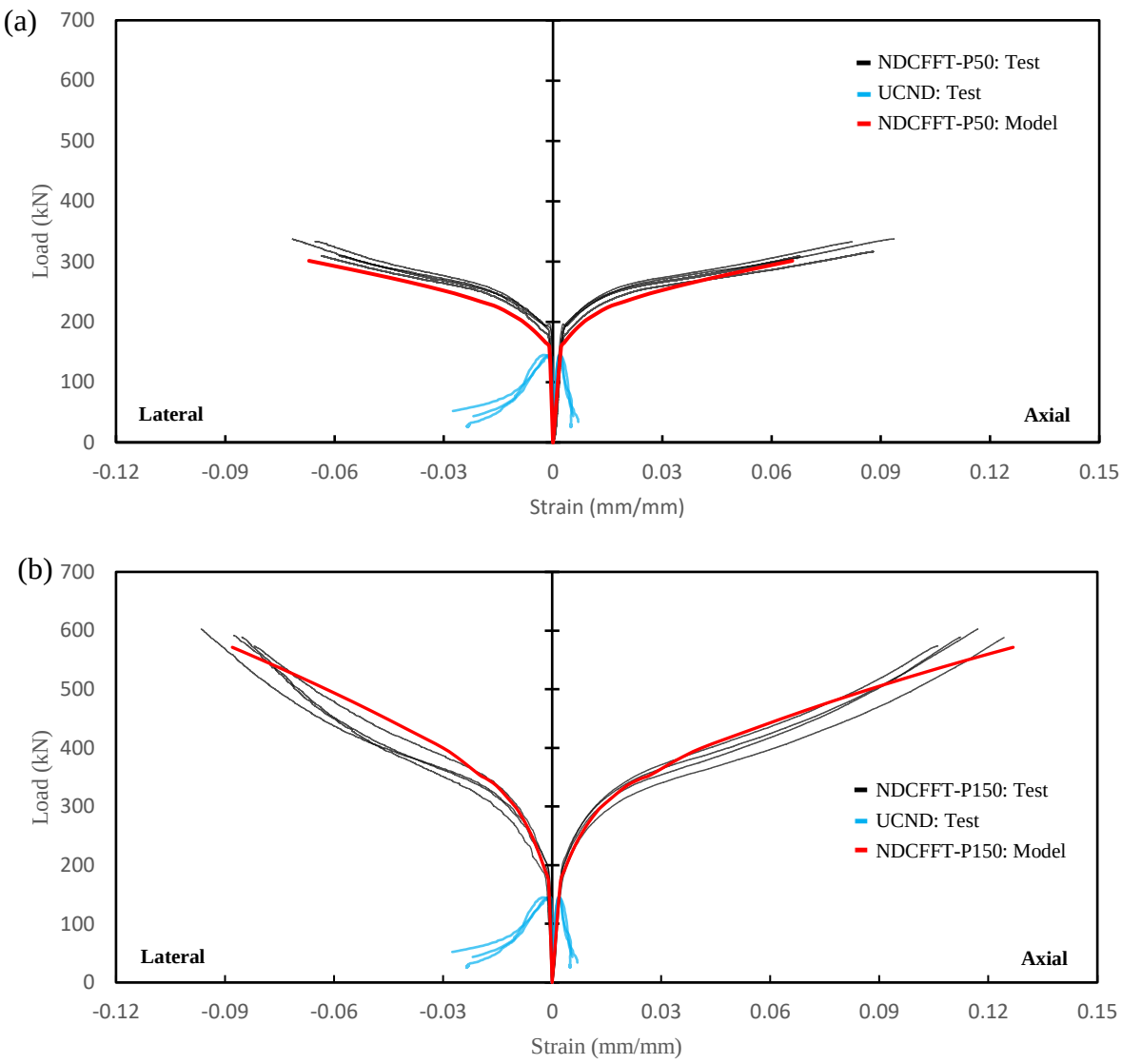

Figure 9. Comparison of the ND CFFT's axial compressive behavior between the nonlinear experimental response and the modified prediction model: (a) thin-walled NDCFFT-P50 specimens; (b) thick-walled NDCFFT-P150 specimens.

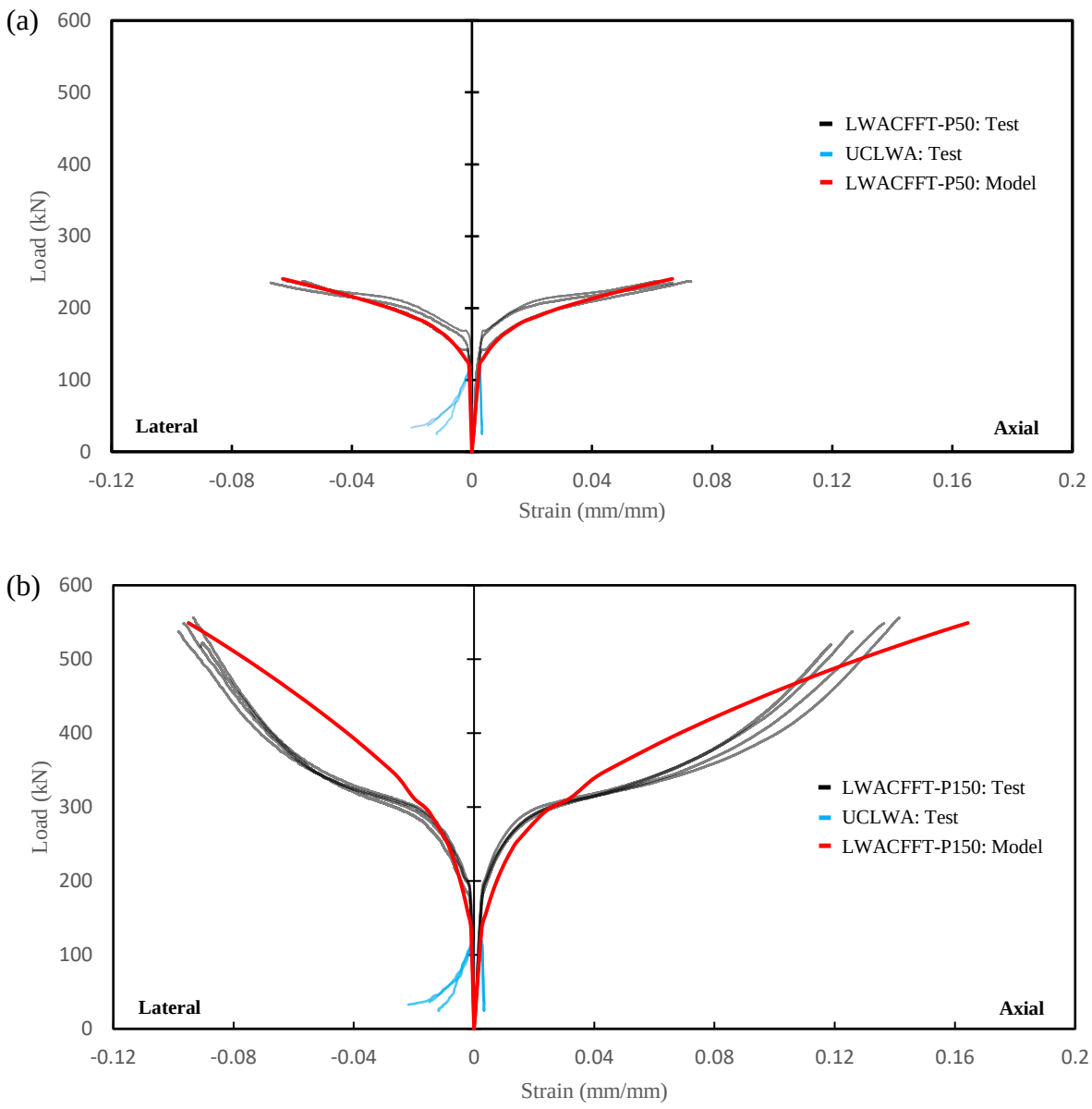

Figure 10. Comparison of the LWA CFFT's axial compressive behavior between the nonlinear experimental response and the modified prediction model: (a) The thin-walled LWACFFT-P50 specimens; (b) The thick-walled LWACFFT-P150 specimens.

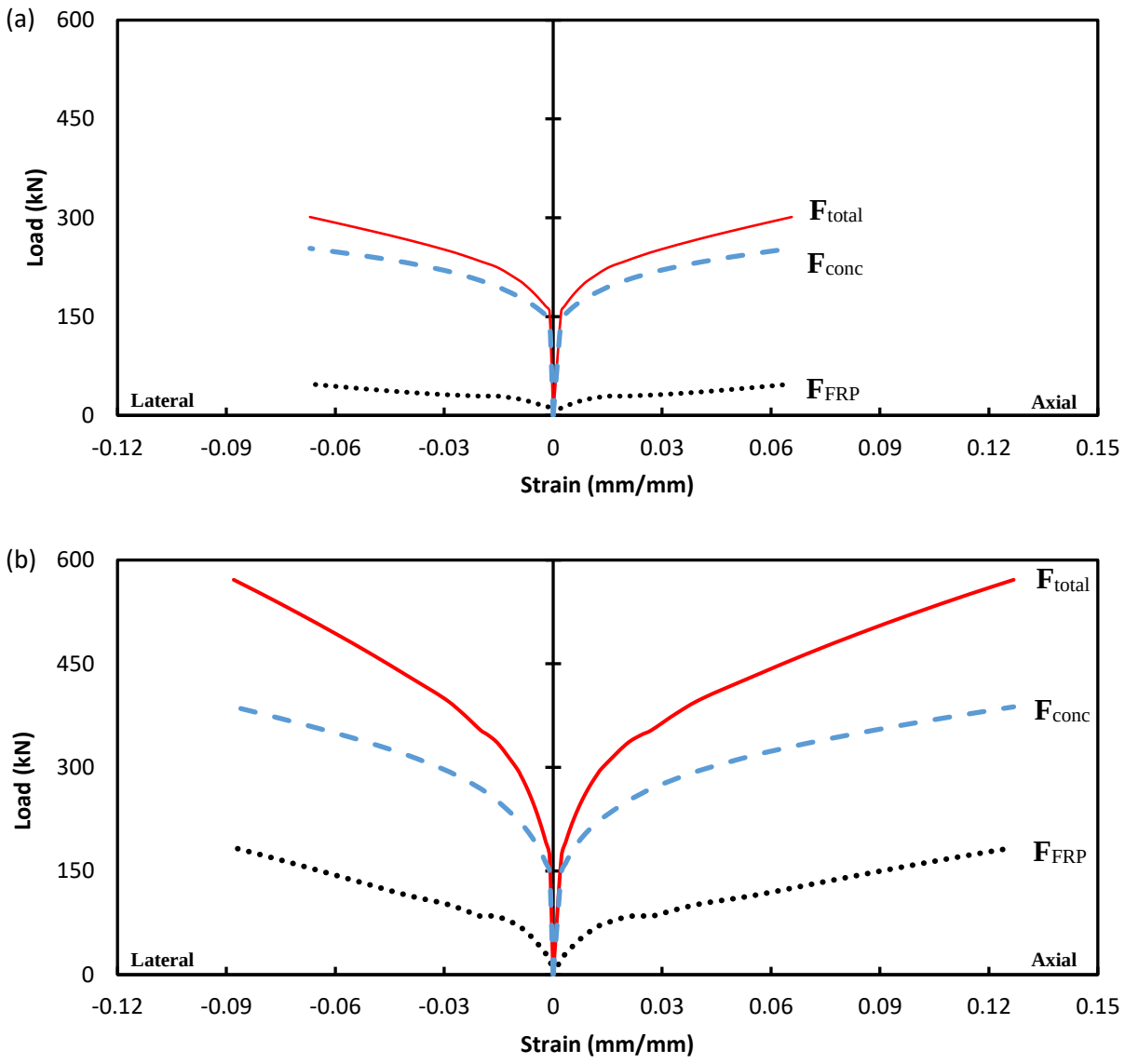

Figure 11. Separate contribution of each CFFT component per Xie et al.'s [6] load-strain modified prediction model: a) NDCFFT-P50; b) NDCFFT-P150.